ANNUAL REVIEWS

Annual Review of Nuclear and Particle Science

Novel Quantum Sensors for Light Dark Matter and Neutrino Detection

Sunil R. Golwala[1] and Enectali Figueroa-Feliciano[2]

[1]Division of Physics, Mathematics and Astronomy, California Institute of Technology, Pasadena, California, USA; email: golwala@caltech.edu

[2]Department of Physics and Astronomy, Northwestern University, Evanston, Illinois, USA; email: enectali@northwestern.edu

Annu. Rev. Nucl. Part. Sci. 2022. 72:419–46

The *Annual Review of Nuclear and Particle Science* is online at nucl.annualreviews.org

https://doi.org/10.1146/annurev-nucl-102020-112133

Keywords

quantum sensing, particle dark matter, neutrinos, particle detectors, superconducting devices, phonons

Abstract

The fields of light dark matter and neutrino physics offer compelling signals at recoil energies of eV to even meV, well below the $\gtrsim$ keV thresholds of many techniques currently employed in these fields. Sensing of such small energies can benefit from the emergence of so-called quantum sensors, which employ fundamentally quantum mechanical phenomena to transduce energy depositions into electrical signals. This review focuses on quantum sensors under development that will enhance and extend the search for "particle-like" interactions of dark matter or enable new measurements of neutrino properties in the coming years.

Contents

1. INTRODUCTION

This review contextualizes and summarizes quantum sensing techniques to detect meV–keV energy depositions for the study of dark matter (DM) and neutrino physics. Our goal is to orient particle and nuclear physicists who may be drawn to this regime by the open questions and exciting techniques, as well as condensed matter and quantum information science (QIS) physicists who are seeking fertile ground for their expertise. Four developments in recent years have been foundational:

- Partly in response to the nondetection of DM directly or at the LHC, the past decade has seen a vast broadening of the spectrum of DM candidates deemed worthy of attention, in particular those that would deposit meV–keV energies.
- Prospects for addressing long-standing open questions in neutrino physics—are neutrinos Majorana or Dirac, what is their absolute mass scale, do they have interactions not explained by the Standard Model (SM) of particle physics, and what might we learn from the cosmic relic neutrino background?—would improve with the capacity to detect meV–keV energies.

- Recognizing the insufficiency of conventional particle detection techniques, particle physicists, especially theorists, have done the atomic, molecular, and optical (AMO) physics and condensed matter physics (CMP) to provide guidance on detection modalities, detection medium choice, and even development of new materials with particularly appropriate excitation spectra.
- QIS techniques have grown in maturity and accessibility over the past decade, and federal and private QIS funding initiatives have accelerated this process and expanded experimental capacity.

This review is structured as follows. Section 2 places the meV–keV energy deposition regime in the broader context of quantum sensors for high-energy physics (HEP). Section 3 reviews the DM and neutrino physics that motivates detection of such energies. Section 4 describes the quantum *sensors* thus far seen as applicable to this energy regime. Section 5 discusses how quantum sensors are being combined with detection media to realize *detector* architectures. Section 6 discusses how QIS techniques can provide sensor readout approaching and exceeding the standard quantum limit (SQL). Brevity requires this review to be primarily qualitative; we seek to orient the reader rather than provide detailed analysis of operation modes, sensitivity, and scalability.

2. QUANTUM SENSING REGIMES AND THE SCOPE OF THIS REVIEW

Quantum sensing becomes a useful technique when searching for the shadowy touch of HEP phenomena on low-energy systems. The US Department of Energy Office of Science's 2019 Workshop on Basic Research Needs for HEP Detector Research and Development (1) provided an excellent summary of how different quantum sensing techniques are applicable to low-energy searches for HEP phenomena (see **Figure 1**). In the mass regime below roughly 1 meV/c^2 (QS1, QS2, and half of QS3), HEP phenomena manifest as weak, (semi-)classical fields whose presence can be sensed via precision measurement techniques drawn from AMO physics, CMP, and/or QIS. Our focus in this review, by contrast, is the regime above ~1 meV/c^2, QS4, where HEP phenomena manifest in a "particle-like" manner. In some cases, the signature is absorption by normal matter of a new light boson in the meV/c^2–keV/c^2 range that exists as the DM and/or can be produced in the lab. In other cases, it is meV–keV energy deposition via scattering, mediated by a new particle, of an already weakly interacting (and possibly new) particle (neutrinos or DM). We focus on techniques applicable to both.

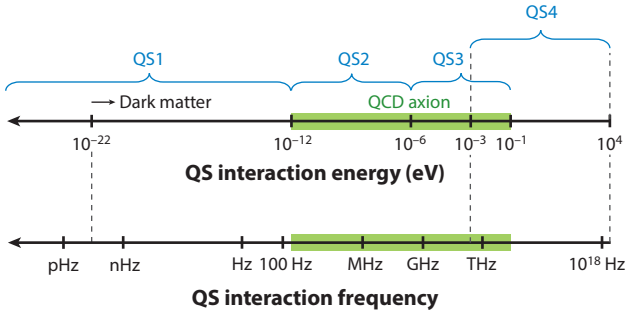

Figure 1

Organization of quantum sensor research for high-energy physics into four energy ranges (QS1–QS4) based on typical absorbed or scattered energy or energy associated with a frequency (1). QS3 and QS4 use different techniques but partially overlap in energy. QS4 is the topic of this review. Figure adapted from Reference 1.

The distinction between QS4 and more conventional sensing of particle interactions is graded. At the boundary is the single-quantum limit for excitations already in broad use by HEP (e.g., detection of single scintillation photons with photomultiplier tubes or their modern successors), where the distinction is not large, either in energy range or in sensitivity limiters—generally, thermal creation of excitations, not quantum fluctuations. Just beyond is the use of lower-energy excitations (e.g., phonons, superconducting quasiparticles) but in a continuum regime—work that has been pursued for decades yet falls under QS4 because the sensing technology overlaps QIS. Firmly in the "quantum sensor" regime are efforts to detect individual low-energy excitations, which generally become limited by truly "quantum" fluctuations and require application of QIS techniques to reach and/or circumvent.

3. SCIENTIFIC MOTIVATIONS: SEARCHING FOR PHYSICS BEYOND THE STANDARD MODEL IN DARK MATTER AND NEUTRINOS VIA meV–keV ENERGY DEPOSITIONS

3.1. Dark Matter

The astronomical and cosmological evidence for DM is extensive and multifaceted (see, e.g., 2; for an excellent, historically oriented review, see 3), and that evidence places important constraints on its properties (see, e.g., 2). We focus here on how DM's properties and potential interactions with normal matter inform the use of quantum sensors.

3.1.1. Required dark matter properties. If DM is a particle, cosmological observations require it to be nonbaryonic and to have been completely or almost completely nonrelativistic ("cold" or "warm," respectively) at the time overdensities started to collapse and structure formation began, which occurred when the matter and radiation densities were equal (redshift $z \approx 3{,}400$). These two properties ensured that structure formation began early enough to yield the amplitude of large-scale structure we see today. For DM masses $\gtrsim$ a few keV/c^2, thermal production in the early Universe would have been viable because residual thermal velocities at matter–radiation equality would have been small enough to satisfy the cold/warm criterion.[1] Conversely, below this mass, production must have been nonthermal. In addition, Pauli exclusion places the constraint that fermionic DM simply cannot "fit" in the phase space of a typical galaxy for $m_{\rm DM} \lesssim$ a few keV/c^2, so only bosonic DM is allowed below this mass.

A last *property* (not a requirement but rather an observation based on the local DM density) is that the particle DM occupation number—the number of DM particles in a volume equal to the DM de Broglie wavelength—is larger than unity if the mass is $\lesssim$1 eV/c^2. Below $\sim$1 meV/c^2, the occupation number becomes so high that DM behaves more like a (semi-)classical field than a collection of individual particles (4). This lower limit of "particle-like" behavior coincides (intentionally) with the lower end of the mass range considered in this review.

3.1.2. The dark matter landscape. From the 1980s through the 2000s, the most favored candidates for particle DM were weakly interacting massive particles (WIMPs) (5) and QCD axions (6–12). The WIMP would be a Majorana fermion and would have been thermally produced, with "weakly" meaning specifically that its interactions with itself and normal matter proceed via

[1] By "thermal," we mean not just the classic "freeze-out" scenario (thermal equilibrium production in the early Universe, with the relic comoving density becoming fixed when the annihilation rate became smaller than the Hubble parameter, before Boltzmann suppression had its full effect) but also "freeze-in" (later DM creation by reactions occurring in the thermal bath of SM particles).

exchange of heavy mediators at or above the electroweak scale, $\mathcal{O}(100)$ GeV/c^2, generated by whatever new physics lies beyond the SM. The QCD axion, invented to solve the strong *CP* problem, would be a boson produced in the early Universe nonthermally as a (cold) Bose condensate. [The QCD axion would be a natural product of inflation, and thus its discovery would be strong evidence in favor of inflationary scenarios (4).] Both WIMPs and QCD axions remain well motivated, but there has been a recognition by the particle DM community in the last decade that a wider net should be cast. The absence of a WIMP detection or evidence for new physics at the LHC suggests that the focus on electroweak-scale physics may be too restrictive. There is significant interest in "hidden-sector" models in which the DM connects to the SM via a "portal" that consists of weak couplings[2] allowed by symmetry and generated radiatively (4), motivating searches for thermally generated, fermionic DM down to the thermal limit of a few keV/c^2. Laboratory axion searches have only just recently reached the necessary sensitivity to see the QCD axion, in a narrow mass range, so nondetection is not the driver. Rather, the reconsideration of WIMPs has motivated a similar reevaluation of cosmological bounds on the QCD axion mass and led to a more general understanding that bosonic DM (beyond the QCD axion) is viable for all masses down to the 10^{-22} eV/c^2 mass range, a lower limit set by the requirement that the de Broglie wavelength of DM be smaller than the size of dwarf galaxies.

3.1.3. Detecting dark matter with quantum sensors: couplings and kinematics. Fermionic DM could be detectable by scattering with electrons or nucleons via a new mediator particle, which could be light or heavy and could be a vector, axial vector, scalar, or pseudoscalar (4). In some cases, the vector mediator has the same quantum numbers as the photon, motivating "kinetic mixing," $\mathcal{L} \supset \epsilon F^{\mu\nu} F'_{\mu\nu}$, between the SM photon and the new particle, now termed a *dark photon*. For dark photons, the coupling is essentially electromagnetism weakened by a factor ϵ^2. In contrast, bosonic DM couples *directly* to normal matter and hence interacts via *absorption* rather than scattering. Bosonic DM could be a vector or axial vector or a real or complex scalar or pseudoscalar. Most of these couplings, for both fermionic and bosonic DM, are to electron or nucleon number, while the dark photon ("vector portal" to hidden sector) couples to electron or ion charge. There can also be coupling to mass ("Higgs portal" to hidden sector). Some of the couplings are to electron or nucleon spin (axial vector and pseudoscalar mediation), also known as magnetic dipole and anapole couplings. The number, charge, and mass couplings are the analog of "spin-independent" couplings for WIMPs while the spin couplings are the analog of "spin-dependent" WIMP couplings.

Astronomical and cosmological constraints already exclude some of the above options for at least some range of their parameters (primarily mass), but the constraints are sufficiently model dependent that they do not provide precise guidance on detector requirements. Rather, we focus on generic guidance about the energy ranges and cross sections of interest.

We can make rough estimates of energy depositions expected for scattering of fermionic DM in the mass range 5 keV/c^2 to 500 MeV/c^2, between the fermionic thermal limit and the lower limit of masses accessible via nucleon scattering with currently available, "nonquantum" techniques. Assuming *s*-wave scattering (not true in all cases!), the maximum and typical recoil energies are (e.g., 13)

$$E_{\max} = \frac{1}{2} m_{\mathrm{DM}} v_{\max}^2 \quad \text{and} \quad E_0 = \frac{1}{2} m_{\mathrm{DM}} v_0^2 \frac{4\mu^2}{m_{\mathrm{DM}} m_{\mathrm{T}}} \approx \frac{\mu^2}{m_{\mathrm{DM}} m_{\mathrm{T}}} E_{\max}, \qquad 1.$$

[2]These couplings are considered weak because the coupling constant of the relevant term in the effective Lagrangian is small, not because the mediator is heavy.

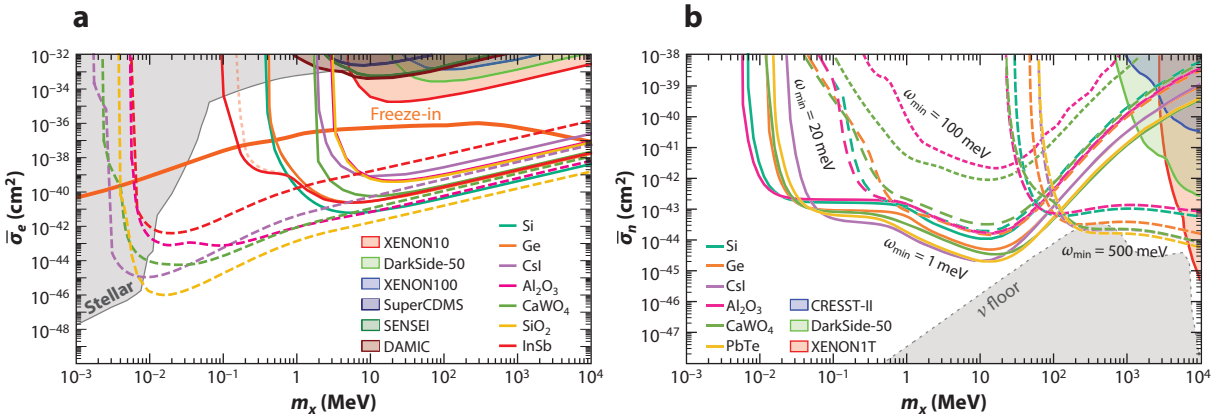

Figure 2

Expected sensitivity of various materials for 1 kg·y exposure for (*a*) electron scattering mediated by a light (low-mass) dark photon and (*b*) nucleon scattering mediated by a heavy ($\gtrsim$400 MeV/c^2) scalar that couples to hadrons primarily. (The plots assume $\hbar = 1$, $c = 1$ units.) Electron scattering uses detection of electron–hole pairs (*solid lines* terminating near 1 MeV/c^2 in panel *a*; Section 5.4) or >1 meV optical phonons (*dashed lines* terminating near 10 keV/c^2 in panel *a*; Section 5.2). "Freeze-in" refers to one dark matter creation scenario. Current constraints from stellar astrophysics ("Stellar") and direct searches (*shaded*, *colored regions* at upper right of each panel) are shown. Nucleon scattering uses conventional nuclear recoils ($[\hbar]\omega_{\min} = 500$ meV; *medium-dashed lines* in panel *b*) and direct creation of acoustic phonons ($[\hbar]\omega_{\min} = 1$, 20, and 100 meV; *solid*, *long-dashed*, and *short-dashed lines* in panel *b*). The "ν floor" region represents an estimate of the sensitivity at which systematic uncertainties on the solar neutrino background become limiting. Figure adapted from Reference 14 (CC BY 4.0).

where $m_{\rm DM}$ is the DM particle mass, $m_{\rm T}$ is the target particle mass, μ is the DM–target reduced mass, $v_0 \approx 10^{-3}c$ is the velocity dispersion of the DM in the halo of the galaxy, and $v_{\max} \approx 2v_0$ is the maximum (escape) velocity of DM. Numerically,

$$E_{\max} \approx \left(2 \times 10^{-6}\right) m_{\rm DM}c^2 = 10 \text{ meV to } 1 \text{ keV}, \quad 2.$$

$$E_0 \approx \left(10^{-6}\right) 2m_{\rm T}c^2 \left(\frac{\mu}{m_{\rm T}}\right)^2, \quad 3.$$

$$\text{DM–electron} : = (1\,\text{eV})\left(10^{-2} \text{ to } 1\right)^2 = \cancel{0.1}\ 1 \text{ meV to } 1 \text{ eV}, \quad 4.$$

$$\text{DM–nucleon} : = \left(\frac{2}{A}\,\text{keV}\right)\left(5 \times 10^{-6} \text{ to } 0.5\right)^2 = \frac{1}{A}\left(50 \text{ neV to } 500 \text{ eV}\right), \quad 5.$$

where A is the atomic mass of the target nucleus in atomic mass units.[3] The motivation for quantum sensors is thus clear: Most of this energy range is well below the keV energies sensed in conventional WIMP detection.

Figure 2 shows two examples of parameter space for DM candidates; the main goal is to convey what magnitude of exposure is necessary to test specific targets. For electron scattering, current constraints are based on exposures as small as a few gram-days, while the projected sensitivities for both electron scattering and nucleon scattering are for 1 kg·y.

[3] Electrons are not at rest ($v_e \approx \alpha Z \gtrsim 10^{-2}c$), replacing one power of $v_0 \approx 10^{-3}c$ with $v_e \approx 10^{-2}c$ and increasing the lower limit of the energy range to 1 meV at $m_{\rm DM} = 5$ keV/c^2 for electron scattering.

3.2. Neutrino Physics

Measurements from neutrinos produced in the Sun (15, 16), atmosphere (17), nuclear reactors (18, 19), and particle accelerators (20, 21) show that neutrinos change flavor as a function of energy and distance traveled. The combined data can be explained only by a model in which at least two of the neutrino species have nonzero, differing masses and the neutrino flavor eigenstates ν_e, ν_μ, and ν_τ are linear combinations of the neutrino mass eigenstates ν_1, ν_2, and ν_3. The three flavors of neutrinos mix via the transformation $\nu_\alpha = U_{\alpha i}\nu_i$, where $\alpha = e$, μ, or τ; $i = 1$, 2, or 3; and $U_{\alpha i}$ are elements of a unitary 3×3 mixing matrix.

With masses implied by flavor oscillations, neutrinos are the only *detected* particles with measured properties not predicted by the SM. Precision measurements of neutrino properties may guide us to the new physics that explains the otherwise-mysterious aspects of the SM. Although neutrino detectors have historically been far away from the quantum regime, we review a range of topics in neutrino physics that can benefit from quantum sensors. In some cases, very small energy depositions must be sensed. In others, energy resolution and/or timing information determines sensitivity, and thus the excellent resolution and fast response of quantum sensors may be useful.

3.2.1. Direct neutrino mass measurements. Oscillation experiments prove that neutrinos have mass but cannot determine the scale of the neutrino mass, only the differences between the squares of the masses. Even the ordering of the mass eigenstates is not yet certain; a robust experimental search is ongoing to determine whether $m_1 < m_2 < m_3$ (the normal hierarchy) or $m_3 < m_1 < m_2$ (the inverted hierarchy). A measurement of $0\nu\beta\beta$ would constrain the Majorana mass ($m_{\beta\beta}$) of neutrinos, but the relationship between this mass and the neutrino mass eigenstates is nontrivial:

$$m_{\beta\beta} = (U_{ei})^2 m_i = \cos^2\theta_{13}(\cos^2\theta_{12}\, m'_1 + \sin^2\theta_{12}\, m'_2) + \sin^2\theta_{13}\, m'_3, \qquad 6.$$

where U_{ei} is the e row in the neutrino mass matrix, $i = 1, 2, 3$ is the mass index, θ_{ij} are the neutrino mass mixing angles, and $m'_i = e^{i\phi_i} m_i$, where ϕ_i are related to CP-odd phases in the neutrino mass matrix (for full details, see 22). The Majorana mass is a complex parameter, and $0\nu\beta\beta$ experiments are sensitive only to its magnitude. To complete the picture, we need a direct measurement of the neutrino mass, which is most accessible by measurements of the spectra from beta decay or electron capture (for a full review, see 23 and references therein).

Most efforts to directly measure the neutrino mass measure the spectrum of either tritium beta decay or holmium electron capture. In the case of tritium, the signal is a deficit of events near the endpoint of the decay at 18.591 keV. The difference between the expected endpoint and the measured endpoint would correspond to the neutrino mass scale m_β, which is approximately the m_1 mass eigenstate value. The KATRIN experiment has placed a limit on the value of the neutrino mass scale to be less than 1.1 eV/c^2 (24). A new method using cyclotron frequency radiation emission spectroscopy seeks to measure the microwave frequency radiation from electrons oscillating in a magnetic field. The power radiated by an 18-keV electron in a 1-T magnetic field is about 1 fW. Parametric amplifiers and other low-noise quantum sensor readout techniques (see Section 6) are being investigated to measure these signals.

The holmium electron capture endpoint is at 2.858 keV and has a similar signal comprising a deficit of events near the endpoint. The shape of the electron capture spectrum is not trivial, but much progress has been made in its theoretical and experimental determination. These experiments use a calorimetric technique where the holmium is embedded in a cryogenic calorimeter. Excellent energy resolution and fast signals are required to resolve the endpoint spectrum and to veto potential backgrounds from pileup.

3.2.2. Nonstandard interactions of neutrinos via coherent elastic neutrino–nucleus scattering. In 1974, Daniel Freedman (25) proposed that, for sufficiently small momentum transfers, the neutrino would interact coherently with the entire nucleus through the neutral-current channel, an interaction analogous to the spin-independent DM–nucleus interaction. The process, dubbed coherent elastic neutrino–nucleus scattering (CEνNS), has a cross section about a hundred times larger than that of inverse beta decay (IBD), the mechanism used in the original neutrino discovery experiment (26). In 2017, CEνNS was experimentally detected for the first time by the COHERENT Collaboration at the Spallation Neutron Source (SNS) at neutrino energies of ∼30 MeV (27). An initial 6.7σ detection was obtained using 14.6 kg of sodium-doped CsI scintillator, which received around 16 keV of energy per neutrino interaction and produced ∼14 scintillation photons per neutrino, detected using photomultipliers. Recently, the CsI measurement has been improved upon with a larger data set and reduced systematics to an 11.6σ detection (28), and 3σ evidence for CEνNS with a 24-kg active-mass liquid argon scintillator detector has also been obtained (29).

New physics, such as dark sector mediators, an anomalous neutrino magnetic moment, and sterile neutrinos, will modify the CEνNS spectrum from the SM prediction. Using an effective field theory treatment, one can encode new physics into a framework of nonstandard interactions of neutrinos (νNSI) (30). Precision measurements of the CEνNS spectrum provide a new avenue to search for νNSI (31). Reactor antineutrinos are a compelling source for this type of search because the neutrino flux from a commercial reactor is 10^5 times that of the SNS. The characteristic $\mathcal{O}$(MeV) energies of reactor antineutrinos translate to nuclear recoil energy depositions from CEνNS in detectors of $\mathcal{O}$(0.1–1) keV, which have so far prevented high-significance detection at these sites. Detectors with low threshold (ideally $\lesssim$10 eV) are required, and fast timing enhances background rejection via anticoincidence with a muon veto.

CEνNS can also set constraints on ^{8}B, CNO, and *pp* solar neutrino fluxes (32) and/or constrain νNSI (33–37). However, compared with the small detectors considered here, a future LXe experiment (e.g., DARWIN) would measure, with far better statistics, ^{8}B neutrinos via CEνNS and the *pp* chain via ν-*e* scattering.[4] Even if one instead assumes a future precise *pp* flux measurement as an input to a solar neutrino CEνNS constraint on νNSI using the detectors discussed here, reactor experiments offer more statistical precision: A 10% measurement of the *pp* chain via CEνNS requires $\mathcal{O}$(50) kg·y exposure with a threshold $\mathcal{O}$(1) eV (38).

3.2.3. Detection of cosmic relic neutrinos. Photons from the cosmic microwave background (CMB) were able to free-stream through the Universe when their mean free path increased suddenly due to the formation of hydrogen and helium from the primordial plasma at recombination, 300,000 years after the Big Bang. They are imprinted with information about the Universe at that early stage, providing us with one of the most informative and precise probes of cosmology. Information from before recombination can be inferred from the study of Big Bang nucleosynthesis, ∼200–1,000 s after the Big Bang. Neutrinos decoupled from other particles in the Universe around 0.3–1 s after the Big Bang, and like the CMB, those initial free-streaming neutrinos cooled as the Universe expanded. They have an estimated temperature today of 1.9 K, forming the cosmic neutrino background (CνB). The study of the CνB can thus probe the earliest moments of our Universe.

The energy of neutrinos from the CνB is $\mathcal{O}$(0.1) meV. Their average velocity is $v_\nu \geq 19{,}600$ km s^{-1} (0.1 eV/c^2)/m_ν. There are several proposals for how to measure the CνB (39). The best prospect

[4]The *pp* chain measurement requires control of ^{136}Xe backgrounds.

is through IBD of tritium. The PTOLEMY project (40, 41) proposes 100 g of tritium infused in a two-dimensional graphene structure. Electrons from the CνB IBD exit the graphene and enter a vacuum space permeated by a magnetic field that filters the electrons, allowing only those very close to the endpoint energy to proceed to a transition-edge sensor (TES) microcalorimeter array (see Section 4.1). These electrons will have an energy of $\mathcal{O}$(1–10) eV, and the detector energy resolution goal is less than 0.05 eV. Thus, detectors with meV resolution are very much of interest to CνB searches.

4. QUANTUM SENSORS APPLICABLE FOR SENSING meV–keV ENERGY DEPOSITIONS

This section describes options for the fundamental sensing element that generates an electrical signal from the final products of the initial energy deposition.

4.1. Transition-Edge Sensors

A TES is a superconducting film operated in its normal–superconducting transition.

4.1.1. Transition-edge sensor concept. Energy coupled to the TES film raises its temperature, which causes a rise in its resistance. The TES is coupled to a superconducting quantum interference device (SQUID) (42) via a series inductor and biased with a DC or AC current through a parallel shunt resistor with $R_{sh} \ll R_{TES}$, yielding an approximate voltage bias. The change in resistance causes a change in the impedance of the TES, which causes a detectable current change in the SQUID. The parameter $\alpha = \frac{T}{R}\frac{dR}{dT}$ characterizes the sharpness of the transition; higher α usually leads to greater sensitivity. Typical transition widths are $\mathcal{O}$(1) mK. TES films are made from a variety of materials, often using the proximity effect or paramagnetic impurities to tune the critical transition temperature (T_c). Mo/Au, Mo/Cu, Ti/Au, Ir/Au, Ir/Pt, Al/Mn, Ir, W, and other combinations of elements have been used. Typical film thicknesses are $\mathcal{O}$(100) nm, and they range in size from a few to hundreds of micrometers to a side. In some designs, a single rectangular film is used, while in others, up to hundreds of TESs are wired in parallel to make a single TES readout channel.

4.1.2. Transition-edge sensor resolution. A particle or photon interacting with the TES places the system far from thermodynamic equilibrium. In the limit in which the energy is rapidly thermalized in the TES (e.g., a direct photon absorption), the response and resolution of the TES will depend on its heat capacity (which determines the size of the temperature increase from the absorbed energy) and the time constant for energy to decouple from the TES thermal system through conduction, radiation, down-conversion, or other processes. Neglecting noise terms from the readout circuit (which can generally be made subdominant), the TES energy resolution can be simplified to

$$\sigma_E = \sqrt{\frac{4k_B T_c^2 C}{\alpha}}\sqrt{\frac{n}{2}}, \qquad 7.$$

where T_c is the transition temperature, C is the heat capacity of the TES system, and n is a thermal conduction exponent of $\mathcal{O}$(1). As described in Section 5, the TES is often coupled to a target. This equation still holds for systems where the TES is measuring the temperature of a target over times that allow the target-TES system to come into quasi-equilibrium. This is the thermal phonon regime (see Section 5.3). Photon spectrometers often operate in this regime. An example is shown in **Figure 3**.

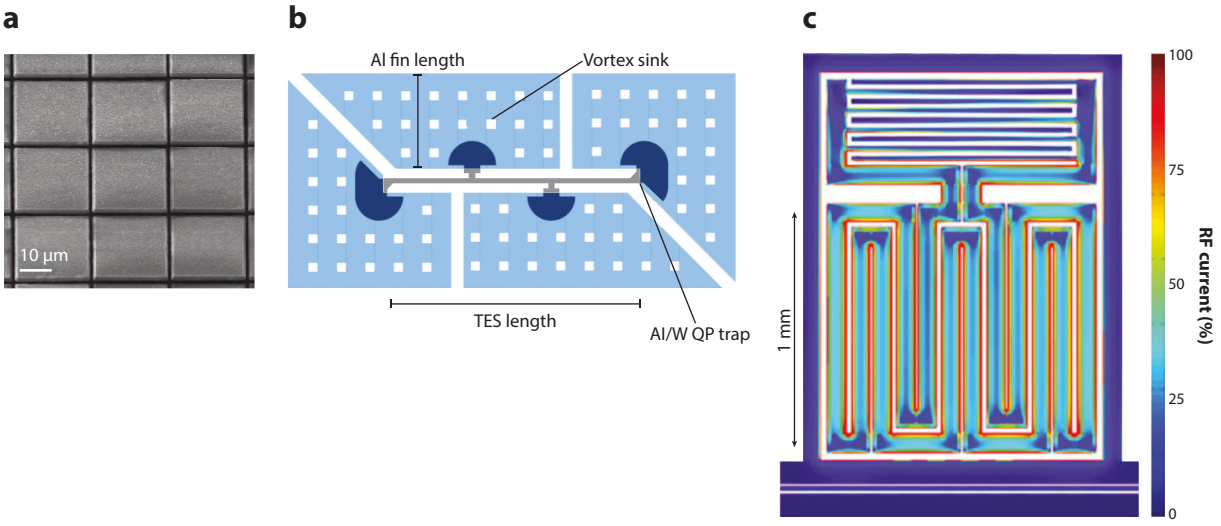

Figure 3

(*a*) A 0.25-eV-resolution transition-edge sensor (TES) array with 50-μm absorbers operating in the thermal regime (Section 5.3). Panel adapted with permission from Reference 43. (*b*) TES design that uses quasiparticle (QP) trapping to collect athermal phonon energy from the substrate (Section 5.2). Athermal phonons transmitted from the substrate break Cooper pairs in the Al (*light blue*), creating QPs. The QPs diffuse about the Al and may be trapped in the Al/W region (*dark blue semicircles*) because it has lower gap energy. There, they deposit most of the Al gap energy into the TES (*thin gray horizontal bar*). The "vortex sinks" provide nonsuperconducting regions for magnetic flux to penetrate through the plane of the film; without such sinks, such flux concentrates into vortices that suppress the superconducting gap and thus act as traps for diffusing QPs. Panel adapted with permission from Reference 44. (*c*) Example of a kinetic inductance detector (KID) design with $f_r = 3$ GHz. The meandered portion is the inductor, while the interdigitated portion is the (insensitive) capacitor. The three lines at the bottom are the coplanar waveguide readout feedline, to which the KID is inductively coupled. The ground electrode extends around the KID to improve isolation from nearby KIDs (45). The color scale shows the variation of the radio frequency (RF) current, indicating that the inductor is largely a lumped element. KIDs may also be designed as transmission-line resonators (see Section 4.2). Panel adapted with permission from Reference 130.

In many designs (especially for rare event searches for which one desires a large target mass), it can be advantageous to collect the energy deposited in the target into the TES before that energy thermalizes and causes an overall temperature rise (Section 5.2). Energy from athermal excitations is funneled into the TES (e.g., using quasiparticle trapping from superconducting structures connected to the TES). An example of such an athermal design is shown in **Figure 3*b***.

4.1.3. Transition-edge sensor multiplexing using superconducting quantum interference devices. The mass/exposure requirements for DM and neutrino applications of TES devices can be achieved through the use of readout multiplexing techniques. Several time-division and frequency-division SQUID multiplexing techniques are being developed (46–49), with microwave SQUID multiplexing (50) for CMB applications providing multiplexing factors of 512 devices per readout channel (51).

4.2. Kinetic Inductance Detectors

A kinetic inductance detector (KID) is a superconducting thin film resonator whose resonant frequency and quality factor change in response to energy deposition.

4.2.1. Kinetic inductance detector concept. In a superconductor, electrons form Cooper pairs, with $2\Delta \sim$ meV binding energy, via a phonon-mediated interaction. These Cooper pairs

carry electrical current without scattering, giving rise to perfect DC conductivity. When subjected to an oscillating field, however, the pairs' inertia (mass) causes them to take some time to respond, yielding an inductive component of conductivity and thus of the surface impedance [$Z_s = (\sigma\, t)^{-1}$] of a thin film (tens of nanometers thick). If an energy deposition breaks Cooper pairs, this inductive impedance changes (an increase because the remaining pairs must speed up to maintain the same Meissner-effect shielding current), and the resulting quasiparticles (analogous to free electrons, though subtly different) increase the dissipative component of the impedance. A KID consists of such a film incorporated into an LC resonator: Monitoring of its resonant frequency f_r and quality factor Q_r recovers these impedance changes (52). KIDs initially were made from quarter- or half-wave lengths of transmission line (53, 54), and, soon after, lumped element designs were demonstrated (55) (**Figure 3**).

KID response is fundamentally proportional to quasiparticle *density*, not number, and thus it scales as the inverse of the volume, introducing a trade-off between volume and threshold. As with TESs (Section 4.1), the trade-off can be mitigated with quasiparticle trapping, though it adds fabrication complexity, and it is not yet clear whether it is necessary (Sections 4.2.3 and 4.2.4). **Figure 3** shows a KID suitable for sensing athermal phonons from a substrate without trapping.

4.2.2. Kinetic inductance detector multiplexability and readout. Superconductivity provides KIDs with a high internal quality factor, $Q_i > 10^5$–10^7: In principle, there is dissipation due only to the exponentially Boltzmann-suppressed thermal quasiparticle population, though other loss mechanisms (superconductor nonidealities, nearby dielectrics) can be limiting. This high Q_i enables frequency-domain multiplexing at tens of MHz to GHz [radio frequency (RF)] via simultaneous monitoring of KIDs at different f_r coupled capacitively or inductively to a single feedline (see **Figure 3**). For example, ∼1,000 resonators with $Q_r = 20{,}000$ spread over 4–6 GHz can be coupled to the same feedline with ample frequency separation ($10\Delta f = 10 f_r/Q_r = 2$ MHz), yet each provides 100 kHz of signal bandwidth, enough to obtain information on the microsecond timescale. Aside from a readily available cryogenic low-noise RF amplifier, the complexity of the readout is entirely in the room-temperature electronics that generates the probe tones and demodulates the KID response from them. Probe tunes are generated by a fast digital-to-analog converter (hundreds-of-megahertz bandwidth, 16 bits) and, if necessary, upconverted to RF using an analog in-phase and quadrature (IQ) mixer. The reception side incorporates an analogous downconversion step followed by digitization with a fast analog-to-digital converter (same bandwidth, ≥12 bits). Demodulation of the KID response can then be performed in field-programmable gate array (FPGA) firmware or a graphics processing unit (GPU) via digital multiplication or fast Fourier transform. Several such platforms exist (e.g., 56–60), and RF System-on-Chip architectures promise to provide this functionality in a commercial package.

4.2.3. Kinetic inductance detector fundamental sensitivity. Generation–recombination noise—Poisson fluctuations on the thermal quasiparticle population—sets the fundamental KID sensitivity. Because the Cooper-pair-binding energy implies a gap Δ in the superconductor density of states (quasiparticles are a "gapped excitation"), this noise should decrease exponentially with temperature, potentially enabling sensitivity to single Cooper-pair breaking ($E \geq 2\Delta$; ∼0.34 meV in aluminum) and thus meV energy depositions.

4.2.4. Kinetic inductance detector sensitivity challenges. One challenge for KIDs is obtaining this exponential thermal quasiparticle suppression. Even though $hf_r \ll 2\,\Delta$, the probe tone can break Cooper pairs via multiphoton absorption (61–63). Other potential Cooper-pair-breaking mechanisms include ionizing radiation; vibrations (via athermal phonons; Section 5.2);

gap spatial variation leading to localized, long-lived quasiparticle traps (64, 65); and blackbody radiation from the cryostat and/or the readout coaxial cables (66). All may need to be mitigated.

The other challenge is readout noise. Two-level-system dielectric noise that manifests only in f_r (e.g., 67–70) can be circumvented by measuring the Q_r signal, but even the best semiconducting cryogenic amplifiers have noise temperatures of approximately 2 K, limiting KID sensitivity well short of the single-quasiparticle level. Superconducting parametric amplifiers (Section 6) improve on this significantly with an SQL (Section 6) noise temperature of ∼0.2 K at 4 GHz, but reaching single-quasiparticle sensitivity likely requires a more strongly QIS-guided approach (Section 6).

4.3. Superconducting Nanowire Single-Photon Detectors

A superconducting nanowire single-photon detector (SNSPD) consists of a thin, narrow superconducting meander able to detect single photons at UV, optical, and/or IR wavelengths.

4.3.1. Superconducting nanowire single-photon detector operating principle. An SNSPD consists of a narrow [$\mathcal{O}$(100) nm wide] superconducting thin [$\mathcal{O}$(10) nm] film, often patterned into a meander structure over the active detection area, biased with a current close to ($\gtrsim$90% of) the superconducting critical current. When a photon is absorbed, it temporarily suppresses the superconducting state near the absorption event. A 1-eV photon will break hundreds of Cooper pairs since their binding energy is $\mathcal{O}$(meV). A resistive hotspot is formed in the wire, which grows as a result of Joule heating. Current is thus forced into a readout circuit placed in parallel to the SNSPD, generating a detectable signal. The reduced current in the SNSPD and heat flow from the SNSPD into the substrate allow the resistive spot to cool and disappear, bringing the detector back to its quiescent state. The response time of these devices can be as small as a few nanoseconds, and the timing jitter can be less than 10 ps. Optical cavities, lenses, fibers, and photonic waveguides are often used to obtain high system detection efficiency.

4.3.2. Applications. SNSPDs have become essential tools in the quantum photonics field and other photon-starved applications (for reviews, see 71, 72). SNSPDs have demonstrated dark count rates of 10^{-4} Hz and energy thresholds of 250 meV, thus making them very attractive detectors for electron-scattering and dark-photon DM (73). Since these devices are approximately two-dimensional, directional detection to search for diurnal modulation (Section 5.1.3) could be achieved by stacking SNSPDs and detecting electrons ejected from one SNSPD into an adjacent one. Current research directions include improving the detection efficiency at lower energies and investigating methods for multiplexed readout (71), which will be required to obtain $\gtrsim$ gram-day exposures.

4.4. Superconducting Qubits

While many types of superconducting quantum bits (qubits) exist, we focus here on those using Cooper-pair boxes (CPBs).

4.4.1. Resonator/Cooper-pair-box-based qubits. A CPB is a very small volume (<1 μm^3) of superconductor coupled by a sub-micrometer Josephson tunnel junction or junctions[5] ($C_J \sim$ fF) to a superconducting reservoir held at ground voltage (see **Figure 4**). In isolation, the CPB

[5] A tunnel junction is a junction between two metals with a thin (a few nanometers) insulating barrier to prevent ohmic current flow. The term "Josephson" indicates that Cooper pairs, as well as quasiparticles, can tunnel through the barrier.

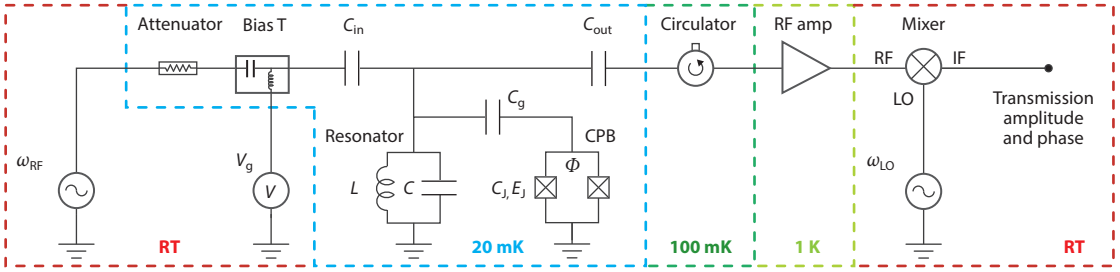

Figure 4

Original resonator-coupled Cooper-pair box (CPB) qubit architecture. The CPB is coupled to a superconducting reservoir by two Josephson tunnel junctions as well as to a half-wave transmission line resonator by placement at its voltage antinode, yielding the equivalent circuit shown in the figure. A DC voltage V_g applied via the bias tee and capacitive divider (effective capacitance C_g^*) sets the offset charge of the CPB, $n_g = V_g C_g^*/e$, with $n_g = 1$ creating a degeneracy necessary to realize the Jaynes–Cummings Hamiltonian. The Josephson energy, E_J, depends on the flux bias Φ and affects the qubit level spacing $E_a = \hbar\omega_a$ [as do the charging energy $E_C = e^2/2(C_g + C_J)$ and the CPB offset charge n_g]. The rest of the schematic shows electronics for a quantum nondemolition measurement of the CPB charge state with a probe tone, which involves driving the resonator with a radio frequency (RF) tone and then recovering changes in the resonator frequency due to changes in the CPB state by mixing the transmitted RF with a nearby local oscillator (LO), yielding an intermediate frequency (IF) band signal that can be recorded. The temperatures of the various portions of the circuit are indicated, with "RT" referring to room temperature (300 K). Figure adapted with permission from Reference 76.

Hamiltonian's eigenstates are also charge eigenstates n (74). Introduction of anharmonicity via the Josephson junction(s) causes the eigenvalue spacing to become unequal, rendering any pair of states (especially $n = 0$ and 2) a two-level system uniquely addressable for quantum computational operations. Many implementations monitor and/or control the CPB state by coupling the electric field of a superconducting resonator to the CPB electric dipole moment, which then enables the system to manifest the QIS Jaynes–Cummings Hamiltonian (75, 76). This Hamiltonian permits quantum nondemolition (QND) monitoring of the CPB quantum state: The coupled resonator-CPB system's resonant frequency depends on the CPB charge state n and level spacing $\hbar\omega_a$, yet, with appropriate design and operational choices, measuring the resonant frequency does not collapse the CPB state. A second benefit, critical to scalability, is that this approach shares the multiplexability of KIDs or any superconducting resonator.

4.4.2. Qubit implementation as a sensor: the quantum capacitance detector. To give one example of how to realize the CPB qubit as a sensor, compatible with the architectures in Section 5, we describe the quantum capacitance detector (QCD) (77, 78). It arranges for energy to be deposited in the superconducting reservoir (as for KIDs). Quasiparticles in the reservoir can tunnel into the CPB island, changing n and thus ω_a and thereby shifting f_r. A monitor tone at the preshift f_r will acquire a large phase shift (approaching 180°). The technique has demonstrated sensitivity to single-quasiparticle tunneling events.

The challenge is that, as with KIDs, the ideal gapped behavior is not realized, with a quiescent quasiparticle density appearing in the reservoir. It nevertheless remains possible to detect energy depositions. In Reference 78, the qubit is rendered blind to the quiescent quasiparticle tunneling rate of 8 kHz by sweeping V_g at a frequency faster than this so that the qubit does not reside at its sensitive point long enough to change state. When an energy deposition changes the quasiparticle density, the tunneling rate increases proportionally, and the more frequent tunneling events now can overlap with the time when the qubit is sensitive, perturbing the response to the sweep. Clear separation between photon absorption and background tunneling has been demonstrated for 5-meV (THz) photons, which generate 20 quasiparticles in Al (78).

Limitations of the current technique are that it can sense only $\mathcal{O}(1)$ fractional changes in quasiparticle density, and it is sensitive only to the quasiparticle density near the tunnel junction. Quasiparticle trapping can address the latter at no increase in complexity because the reservoir can also be the energy collector. Certainly, for rare event searches in which mitigation of the quiescent quasiparticle density may be possible, quantum capacitance detectors (and CPB-based qubits more generally) are worth consideration. Future CPB monitoring approaches may circumvent the background tunneling rate limitation and approach generation–recombination noise.

5. DETECTOR ARCHITECTURES USING QUANTUM SENSORS FOR meV–keV ENERGY DEPOSITIONS

5.1. General Considerations

We discuss in this section a number of general considerations for the coupling of quantum sensors to media that act as the particle-interaction target.

5.1.1. Detector mass. The interaction rates discussed in Section 3 motivate detector exposures of gram-days to kilogram-years. The target must therefore have a mass of grams to kilograms and a volume of 1 to 10 cm^3, largely excluding use of the above sensors alone or even assisted by quasiparticle trapping. We therefore focus on architectures with an $\sim$1 cm^3 substrate in which excitations are created and propagate to a sensor or sensors on the surface. The word "detector" refers to the ensemble.

5.1.2. Energy ranges and excitations. The nature of substrate excitations is central to detector design. What excitations are created, and how, is quite energy dependent. Two energy scales enter: the maximum energy of the excitations, E_{ex}^{max}, and the binding energy of electrons or ions to their sites, E_{bind}. Historically in WIMP and neutrino detection, the keV-scale energy depositions of interest were so much larger than the eV-scale binding[6] and excitation[7] energies that E_{bind} and quantization at the E_{ex}^{max} scale could be neglected. Interest in meV–eV depositions necessitates accounting for both, leading (typically) to three regimes:

- $E_{ex}^{max} \ll E_{bind} < E_r$: An electron or nucleus is liberated, and the continuous limit applies to excitation creation, populating the entire excitation spectrum.
- $E_{ex}^{max} \lesssim E_r < E_{bind}$: In this regime, the scattering can still be considered to be with a single electron or nucleus, but the recoiling particle is not unbound. It may or may not be possible to create the excitation of interest. For example, $E_{ex}^{max} \sim E_{bind}$ for ionization and scattering with an electron, so the $E_{ex}^{max} \lesssim E_r < E_{bind}$ condition cannot be satisfied for $E_r < E_{bind}$. When it can be, the excitations can be considered in the continuous limit and the full spectrum populated if $E_{ex}^{max} \ll E_r$; otherwise, only a few may be created.
- $E_r \lesssim E_{ex}^{max}$: In this regime, the interaction is directly with the excitations because the momentum transfer is so small and the corresponding wavelength so large that the momentum is transferred coherently to multiple electrons or ions at once. Only one or a few excitations may be created initially.

In the latter two regimes, one must consider the detailed spectrum of excitations. For scattering with electrons, one must thus invoke the full dielectric loss function of the material to below E_{bind}, and, for scattering with nuclei, one needs the full phonon spectrum.

[6]For example, the electron–hole pair creation energy in silicon is 3.8 eV, and the Frenkel defect energy (energy required to unbind an ion) is 12–36 eV, depending on the direction in which the ion is displaced (79).
[7]The excitation energies are eV for ionization and tens of eV for scintillation.

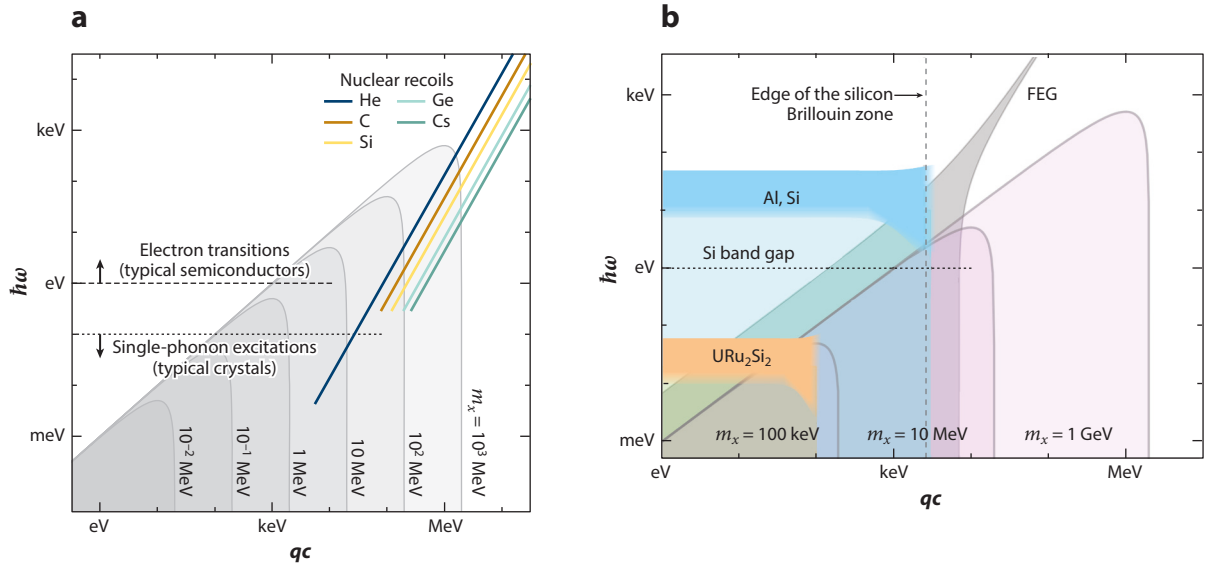

Figure 5

Connection between dark matter (DM) kinematics and detector excitations. The inverted parabolas are the space of energy–momentum transfer accessible for the indicated DM particle mass and $v = 10^{-3}c$. (The q axis is obtained by multiplying momentum by c.) The lines in panel *a* indicate the locus of nuclear recoils for various materials, terminating where scattering can no longer be treated as involving a single nucleus (about an order of magnitude below E_{bind}). Regions occupied by electronic transitions in semiconductors and single-phonon excitations are indicated. In panel *b*, the blue and orange regions indicate the support of the plasmon part of the dielectric loss function for typical (Al, Si) and heavy-fermion (URu_2Si_2) materials. The former has a tail extending into the DM region while the latter strongly overlaps it, indicating that plasmon excitation is feasible. The gray free-electron gas (FEG) region indicates scattering with unbound electrons. The Si band gap is indicated, consistent with panel *a*. The dashed–dotted line marks the edge of the silicon Brillouin zone, below which single-phonon creation becomes viable. Panel *a* adapted from Reference 80 (CC BY 4.0). Panel *b* adapted from Reference 81 (CC BY 4.0).

Figure 5 illustrates the overlap in energy–momentum space between DM and various types of excitations. Measurements with neutrinos, in contrast, typically occupy the $E_r > E_{\text{bind}}$ regime: CEνNS involves neutrinos with energies of 1 to 30 MeV, yielding nuclear recoils $\gtrsim\mathcal{O}(100)$ eV; $0\nu\beta\beta$ yields electron energies above 2 MeV; and, even for 0.1 meV/c^2 cosmic relic neutrinos, the scheme using IBD employs detection of electrons with $\mathcal{O}(10\text{–}100)$ eV. The exception is the detection of ~0.4 MeV *pp* neutrinos, where required thresholds of <1 eV put the detector in one of the latter two regimes, depending on the technology.

5.1.3. Anisotropy. Crystals are inherently anisotropic, and this anisotropy can make the excitation spectrum dependent on the direction of the momentum transfer. Near E_{bind}, the threshold for unbinding an ion or electron can depend on the direction of the momentum transfer (82). In the single/few-excitation-creation regime, $E_r \lesssim E_{\text{ex}}^{\text{max}}$, the sensitivity of the interaction cross section to such anisotropy can become significant (e.g., 80, 83, 84). In some cases, these effects can be as large as tenths of the isotropically averaged interaction rate, which would be a boon for background rejection: DM comes primarily from one direction owing to the Sun's circular orbit through the isotropic DM gas, and this direction rotates in the lab frame daily (diurnal modulation), providing a way to identify a modulating DM signal in the presence of backgrounds fixed relative to the lab frame. Neutrino fluxes are typically directional too. In the case of solar neutrinos, the same diurnal modulation applies. For neutrinos from a reactor or a beam, the source is generally fixed

to the lab frame, eliminating the potential for diurnal modulation but retaining event direction as a discriminator between signal and background.

5.1.4. In-medium effects. Another consideration is "in-medium" effects—effectively, screening. Because the dark photon's interaction with normal matter is via kinetic mixing with the normal photon, it is subject to dielectric screening and effective photon mass effects, codified by the imaginary (lossy) part of the medium's dielectric function. There is some debate in the literature on this topic (e.g., 85 versus 81), leading to different conclusions about how screening degrades the sensitivity of superconductors and whether it also applies to light scalar and nonkinetically mixed vector mediators. Recent work using an effective field theory framework (86) concludes that DM absorption rates for vector (dark photon) and pseudoscalar (axion-like particle) DM can be calculated directly from the dielectric function as in Reference 81, but for scalar DM, the effective field theory framework is required and gives different results from those of previous scalar DM scattering rate calculations (81, 87, 88).

5.1.5. Particle backgrounds. Particle backgrounds at the meV–keV scale differ from those at higher energy because these are the energy scales of condensed matter and atomic physics, not nuclear physics. Conventional keV–MeV backgrounds—including the Compton and bremsstrahlung spectra arising from natural radioactivity, soft (MeV) neutrons from fission and (α, n) reactions, hard neutrons from cosmogenic muons, and betas and daughter nuclei from the radon chain—tend to have flat energy spectra down to low energy (modulo steps and turnoffs due to kinematics), making them distinguishable from the steeply rising spectra of low-mass DM or CEνNS. [Coherent photon scattering with nuclei is a notable exception, rising at low energy (89).] Rather, it is atomic physics secondaries that become challenging. Cosmogenic creation of isotopes that decay by electron capture results in X-rays from atomic shell vacancies (e.g., Ge M-shell at 160 eV). Cherenkov and transition radiation and scintillation/luminescence from metastable atomic states are all viable mechanisms, with the latter likely observed (90) and the former already calculated (91). There are almost certainly additional condensed matter backgrounds to be discovered as thresholds approach the meV level. First-principles surveys of potential new backgrounds should be expanded, and detector architectures will need to respond to them as they arise.

5.1.6. Dark counts. Perhaps one of the biggest challenges, and the one hardest to predict, is so-called dark counts—excitations not created by particle interactions. Already, ionization leakage has begun to plague architectures relying on electron–hole pair detection when moderately high voltages (tens to hundreds of volts) are applied (Section 5.4). Crystal stress and cracking, along with vibrations, have been a problem for even athermal-phonon-based architectures for decades. Sensors based on Cooper-pair breaking have seen "quasiparticle poisoning"—nonthermal sources of quasiparticles—cause departures from Boltzmann suppression of quasiparticle density (Sections 4.2.4 and 4.4.2). Two-level systems in the targets can have long-lived states that relax with time constants much longer than the sensor bandwidth and could become another source of dark counts or excess noise. Predicting, discovering, and addressing these new backgrounds will be crucial to the development of quantum-sensor-based detectors for DM and neutrino physics.

5.2. Athermal Phonons in Crystals

To distinguish athermal from thermal phonons, we assume that the sensor on the surface is sensitive only to phonons above a minimum energy, $E_{\rm ph} > E_{\rm min}$, set in most cases by the Cooper-pair-breaking energy 2Δ, and that this threshold satisfies $E_{\rm min} \gg k_{\rm B}T = 86.5\ \mu{\rm eV}\,(T/1\ {\rm K})$. Given the meV *detector* threshold we seek to achieve, we take $E_{\rm min} = \mathcal{O}(0.1)$ meV for specificity and to

account for losses to $< E_{\rm min}$ excitations (for reference, Al has $2\Delta \approx 0.4$ meV), thus requiring $T < 0.1$ K.

The phonon spectrum depends on the unit cell of the crystal. Even in monatomic silicon, the unit cell has two ions, yielding two phonon modes: acoustic (ions move together) and optical (ions move oppositely). Each mode has three polarizations: two transverse and one longitudinal. The dispersion relations of phonons, $\omega(\vec{k})$, are anisotropic. Acoustic phonons have a dispersion relation $\omega(\vec{k})$ that approaches $\omega = c_s k$ near zero energy, where c_s is the sound speed of the mode. Their maximum energy is approximately $E_{\rm Debye}$, set by c_s and the material density, typically tens of meV. Optical phonons have a much flatter dispersion relation with $E_{\rm ph} \sim E_{\rm Debye}$ and nonzero energy even at $k = 0$. The two correspond to a diagonal line with unity power-law slope and a flat line (at $E_{\rm Debye}$) in energy–momentum space (**Figure 5**).

5.2.1. Creation. We consider the three regimes noted in Section 5.1.2, with $E_{\rm ex}^{\rm max} \sim E_{\rm Debye}$:

- $E_{\rm Debye} \ll E_{\rm bind} < E_{\rm r}$: An electron or nucleus is liberated, and the continuous limit applies. Because $E_{\rm bind} \gg E_{\rm Debye}$, the entire phonon spectrum is populated, with the phonon phase space, $\mathcal{D}(E_{\rm ph}) \propto E_{\rm ph}^2$, favoring higher energies initially. If other excitations are created, those excitations return their energy in phonons when they are collected unless they escape the substrate (e.g., scintillation, evaporated He atoms). Some energy may be stored in permanent crystal defects.
- $E_{\rm Debye} \lesssim E_{\rm r} < E_{\rm bind}$: In this regime, the scattering is still with a single electron or nucleus,[8] but the particle is not unbound. It sheds its energy into phonons (again, populating the entire phonon spectrum) and possibly other collective excitations (e.g., plasmons), but again those other excitations eventually decay to phonons. No defects can be created. There is ongoing work to study this regime, but an exhaustive analysis has not yet been done.
- $E_{\rm r} \lesssim E_{\rm Debye}$: In this regime, the momentum transfer is so small that the interaction is with many unit cells coherently—that is, with phonons themselves. Numerous papers have addressed this regime (14, 80). Again, no defects can be created.

There is a special case, interaction of dark photons with ionic crystals such as sapphire (Al_2O_3) or quartz (SiO_2), in which the unit cell has an electric dipole moment. Dark photons couple to this dipole moment via kinetic mixing with the normal photon, naturally causing oppositely charged atoms to move in opposite directions—an optical phonon. Dark photons thus have an enhanced coupling to ionic crystal optical phonons, though the energy transfer to excitations is unchanged.

5.2.2. Propagation and collection. As athermal phonons propagate in the substrate, they experience anharmonic decay, isotopic scattering, and surface down-conversion.[9] Anharmonic decay, in which one phonon decays to two phonons with rate scaling as $E_{\rm ph}^5$, causes the phonon spectrum to downshift in energy with time (down-conversion). Isotopic scattering, in which phonons scatter off inhomogeneities in the ion mass with rate scaling as $E_{\rm ph}^4$, is elastic and preserves the energy spectrum. Both types of scattering cause diffusive early propagation followed by ballistic propagation once the mean free path becomes comparable to the substrate dimensions ($E_{\rm ph}^{\rm ball}$ with $E_{\rm min} \ll E_{\rm ph}^{\rm ball} \ll E_{\rm Debye}$). At that point, surface-mediated down-conversion, a process that is poorly

[8] $E_{\rm Debye}$ corresponds to q at the edge of the Brillouin zone ($\sim$keV/c), where the wavelength of the momentum transfer is comparable to the size of the unit cell.

[9] For an extensive review on the subject of propagation and collection, see, e.g., Reference 92. This discussion draws from Reference 85.

understood but that appears to depend on surface films and treatment, limits the phonon lifetime as well as reflection specularity. For $E_r \ll E_{Debye}$, only a single phonon or a few acoustic phonons may be created, but the above still largely applies, though the phonons will immediately propagate ballistically if $E_{ph} < E_{ph}^{ball}$.

The lifetime against anharmonic decay to $E_{min} \approx 0.1$ meV can be $\mathcal{O}(1)$ s (85). A 1-s lifetime, combined with a typical c_s on the order of a few kilometers per second, yields $N_{surf} > 10^5$ surface interactions. If isotopic scattering remains important and makes phonon transport quasi-diffusive as E_{ph} approaches E_{min}, N_{surf} may be smaller, but data from SuperCDMS athermal-phonon-mediated detectors suggest that surface-mediated down-conversion dominates in either case, yielding $N_{surf} \sim 1{,}000$ (M. Pyle, personal communication).

The surface sensors can detect the majority of this energy if

$$f_{surf}\, f_{abs}\, N_{surf} \sim 1, \qquad 8.$$

where f_{surf} is the fraction of the surface covered with sensors and f_{abs} is the probability for absorption per interaction with a surface sensor. f_{abs} is determined by acoustic impedance mismatch at the substrate–sensor interface and the probability of breaking a pair in the sensor. The latter is approximately d_{abs}/ℓ_{pb}, where d_{abs} is the thickness of the phonon absorber and ℓ_{pb} is its pair-breaking length. For Al, $\ell_{pb} \approx 1$ μm, and it is generally smaller in other materials. Film deposition places a practical restriction of 10 nm $\lesssim d_{abs} \lesssim$ 1,000 nm. Acoustic mismatch is, at worst, a factor of 0.5,[10] so $f_{abs} \approx 0.01$–1 is a reasonable range. Thus, $f_{surf} = 0.001$–0.1 is required, with $f_{surf} = 0.01$–0.1 conservative and practically achievable.

The energy resolution of such a detector is roughly

$$\sigma_E \approx \frac{\sqrt{N_{sens}}}{\min(f_{surf}\, f_{abs}\, N_{surf}, 1)}\, \sigma_{sens} \sqrt{\frac{\tau_{sens} + \tau_{ph}}{\tau_{sens}}}, \qquad 9.$$

where σ_{sens} is the energy resolution of a single sensor of the type described in Section 4, N_{sens} is the number of sensors on the substrate surface, τ_{sens} is the intrinsic decay time of the sensor,[11] and τ_{ph} is the lifetime of the $>E_{min}$ phonons in the substrate.[12] $\sqrt{N_{sens}}$ accounts for quadrature addition of noise of the individual sensors. $\sqrt{\tau_{sens} + \tau_{ph}}$ comes from a standard optimal filter (93, 94) calculation assuming the sensor noise is white while the phonon signal pulse shape has two poles set by τ_{sens} and τ_{ph}.[13] Given large uncertainties on the other factors, we have neglected a prefactor of ∼0.5 that accounts for the energy lost to $<E_{min}$ phonons in the process of absorbing $>E_{min}$ phonons (95, 96). The quantities in the expression are not independent, and those relationships must be accounted for. The above provides an appropriate framework for optimization of σ_E.

The best performance demonstrated for this style of sensor is at the level of $\sigma_E = 2$–4 eV for tungsten TES-based sensors employing Al athermal phonon collection fins and quasiparticle trapping on an ∼1 cm^3 silicon substrate (44, 97).

5.3. Thermal Phonons

For all three cases described in Section 5.1.2, and irrespective of the type of initial excitations created by an interaction event in the target, the energy in excitations that do not leave the substrate

[10] For instance, diamond (12 km s^{-1}) and Al (3 km s^{-1}) yield about 0.6.

[11] This intrinsic sensor decay time is τ_{eff} for a TES and is the quasiparticle lifetime τ_{qp} for a KID or a CPB.

[12] Ideally, τ_{ph} is determined by phonon collection and destruction in the sensors, $\tau_{ph} = \tau_{coll}$, but surface down-conversion (or even escape to the mounting structure) can dominate.

[13] Rise times do not play a significant role in energy resolution unless they approach τ_{sens} or τ_{ph}.

returns to the phonon system once those excitations return to their quiescent state. If the surface sensor is strongly coupled to the target and does not have a minimum excitation energy of its own (no energy gap), then there is effectively no $E_{\rm min}$ and the sensor maintains quasi-equilibrium with the target (i.e., it samples the full phonon spectrum) from the initial interaction, through phonon down-conversion and relaxation of excited states, to the point at which the system returns to quiescence. In this limit, the threshold is limited only by the thermal excitations as per Equation 7. One requirement for this picture to be valid is that all excitations in the system relax and release their energy to the phonon system with a time constant much shorter than $\tau_{\rm sens}$. Crystal defects are an example of an excitation that is (very) long-lived and would rob energy from the thermal phonon signal.

As discussed in Section 5.1.1, the required exposures motivate detector masses at the gram scale or larger. Extrapolations of the designs used in the NUCLEUS and Ricochet experiments (98, 99) to lower temperatures and/or heat capacities could achieve $\mathcal{O}(100)$ eV resolution. Taking as an example a silicon target of 0.1 g, operated at 15 mK and instrumented with a TES, an evaluation of Equation 7 gives $\sigma_{\rm E} \approx 100$ meV. A 5σ threshold would be 500 meV, low enough to detect recoils creating only one electron–hole pair. An array of such detectors would provide enough mass for a competitive exposure and sensitivity to DM down to 1 MeV/c^2 and 30 MeV/c^2 through electron and nuclear recoil channels, respectively (14). The benefit of thermal phonon detection is that the sensor does not have intrinsic dark counts or suffer from quasiparticle poisoning; thus, in principle, its resolution is dictated by the thermodynamics of Equation 7. However, since the detector is sensitive to the heat capacity of the target, the system heat capacity could become dominated at the lowest temperatures by two-level systems, defects, impurities, surface states, or other unexpected degrees of freedom, which would degrade the intrinsic energy resolution. Lower thresholds would require even smaller-mass targets or lower operating temperatures, increasing the complexity of the experiment.

5.4. Sensing Electron–Hole Pairs in Semiconductors

Creating an electron–hole pair in a semiconductor requires a deposition giving an electron enough energy to jump from the valence band to the conduction band, $E_{\rm r} > E_{\rm bind}$. For direct band gap semiconductors, $E_{\rm bind}$ is just the band gap energy, $E_{\rm g}$. For indirect band gap semiconductors, $E_{\rm bind}$ is larger because the difference in momentum between the valence and conduction states must be supplied as well. For DM, as shown in **Figure 5*a***, kinematics limits the DM mass able to create an electron–hole pair through electron scattering to $m_\chi \gtrsim 0.3$ MeV/c^2 ($E_{\rm bind}$/eV). $E_{\rm g}$ is material specific and can vary from a fraction of an eV (InSb) to ∼10 eV (SiO_2).

Nuclear recoils can create electron–hole pairs for $E_{\rm nr} > E_{\rm bind}$, where $E_{\rm bind}$ is now the ion-binding energy of the material. The number created on average is $N_{\rm eh} = Y(E_{\rm nr}) \cdot E_{\rm nr}/\epsilon$, where $E_{\rm nr}$ is the nuclear recoil energy, ϵ is the average energy to create an electron–hole pair,[14] and $Y(E_{\rm nr})$ is the *ionization yield*. For $E_{\rm nr} < E_{\rm bind} \sim \mathcal{O}(10)$ eV, no electron–hole pairs are expected, and the energy will go directly to the phonon system.

To detect the amount of ionization created in an event, a voltage can be applied across the detector and electrodes connected to sensitive charge amplifiers [using junction-gate field-effect transistors (JFETs) or high-electron-mobility transistors (HEMTs)]. The threshold for these readouts is $\mathcal{O}(100)$ eV, although work is ongoing to improve the resolution of this type of charge readout down to $\mathcal{O}(20)$ eV (100).

[14]It generally holds that ϵ is a few times $E_{\rm g}$ because most of the energy is lost to phonon creation.

Detectors based on Skipper charge-coupled devices (CCDs) (101) have achieved single electron–hole pair resolution and produced world-leading DM results (102, 103). Like regular CCDs, Skipper CCDs accumulate charge in a depleted region at each pixel and then move the charge "packets" from each pixel sequentially to the readout electronics, which reads one charge packet at a time. The Skipper CCD achieves sub-e^- ($0.068e^-$ best to date) resolution by measuring the same charge packet repeatedly (up to thousands of times), shifting it back and forth at high frequency between the sense node and a storage node to mitigate low-frequency amplifier noise.

Another technology that achieves single electron–hole pair resolution relies on the Neganov–Trofimov–Luke (NTL) effect (104, 105). A voltage source is used to apply a drift field to the target. This field quickly accelerates electrons and holes created by a recoiling particle to a terminal velocity near the sound speed due to phonon emission. The work done by the voltage source is thus released into the crystal as phonons. The total energy input to the phonon system is thus

$$E_{\rm tot} = E_{\rm r} + E_{\rm NTL} = E_{\rm r}\left(1 + Y_{\rm e,n}\frac{e{\cdot}V}{\epsilon}\right), \qquad 10.$$

where $Y_{\rm e,\,n}$ is either 1 for electron recoils or the yield $Y(E_{\rm r})$ for nuclear recoils, and $E_{\rm NTL}$ is the $e{\cdot}V$ energy emitted by each charge due to the NTL effect. With $V \gg \epsilon/e$, one obtains phonon-based charge amplification, and single electron–hole pair resolution has been demonstrated (44, 106).

It should be noted that creation of electron–hole pairs by an interaction or by a recoiling particle does not require that they be sensed directly. They can be allowed to recombine, yielding their creation energy in phonons (Sections 5.2 and 5.3). If NTL amplification is not used, however, sensing of single electron–hole pair creation requires a threshold below $E_{\rm g}$ rather than below $e{\cdot}V$.

5.5. Breaking Cooper Pairs in Superconductors

Electron scattering with superconductors can break Cooper pairs directly. The cross section for this process may, however, be attenuated by "in-medium" screening effects, though Section 5.1.4 notes some debate about this. In most models, nucleon scattering would be unscreened, so it remains interesting to consider superconducting targets.

In the generic language of Section 5.1.2, one might expect electrons (quasiparticles) to play the dominant role in superconductors and set $E_{\rm ex}^{\rm max}$, but they do not. Because of the phonon phase space (Section 5.2), a quasiparticle created with $E_{\rm qp} \gg \Delta$ emits phonons $\propto E_{\rm ph}^2$ up to $E_{\rm Debye}$ and relaxes quickly. Even though these energetic phonons can break Cooper pairs, the quasiparticle phase space factor is largely energy independent and even favors final states near Δ because of the density-of-states singularity there. Thus, the phonons set $E_{\rm ex}^{\rm max}$, implying $E_{\rm ex}^{\rm max} = E_{\rm Debye}$.

The excitations that propagate are, however, different. Phonon emission is a scattering process, preventing $E_{\rm qp} \gg \Delta$ quasiparticles from propagating. Athermal phonons with $E_{\rm ph} \geq 2\Delta$ also do not propagate because the pair-breaking length is micrometers or less (Section 5.2). Quasiparticles must thus relax to $\approx\Delta$ to propagate. Athermal phonons below 2Δ, emitted as quasiparticles approach Δ, can propagate without breaking pairs. The majority will be just below 2Δ because of phonon phase space. Thus, while $E_{\rm ex}^{\rm max} = E_{\rm Debye}$, the propagating excitations are quasiparticles and athermal phonons with $E_{\rm ex} \approx 2\Delta$.[15]

If produced in large numbers because $E_{\rm r} \gg E_{\rm ex} = 2\Delta$, quasiparticles and athermal phonons will be partitioned approximately 57%/43% (95, 96). As $E_{\rm r}$ approaches $E_{\rm ex} = 2\Delta$, the distribution will depend on the initial type of recoil and $E_{\rm r}$.

[15] We assign the quasiparticles 2Δ instead of Δ since they are produced in pairs.

Section 5.2 applies to propagation of the sub-2Δ phonons. In fact, these phonons have $E_{ph} \lesssim E_{ph}^{ball}$ for most superconductors and can propagate freely. The sensors to collect them must obviously have $\Delta_{sens} < \Delta_{subs}$, and, if it is desired to separately collect the phonons and quasiparticles, an insulating barrier is needed between the substrate and sensor.[16]

Regarding quasiparticles, Reference 85 shows that, in high-quality crystals of Al, quasiparticles can propagate ballistically for $\mathcal{O}(10)$ ms at hundreds of kilometers per second.[17] For a 5-mm-scale substrate, $N_{surf} > 10^6$. They should be trapped at the sensor as is done with TESs (Section 4.1). An analysis similar to that for phonons (Section 5.2) ensues, now with f_{abs} set by the transparency of the substrate–sensor interface to quasiparticles (mainly due to oxidation) and the mean free path against trapping of an $E = \Delta_{subs}$ quasiparticle in the Δ_{sens} material via phonon emission. Scaling from the measured f_{abs} for the Al/W interface in SuperCDMS-style TES sensors that use quasiparticle trapping (Section 4.1), Reference 85 concludes that $f_{abs} \approx 0.1$ should be easily achievable. To allow for surface trapping, we conservatively set $N_{surf} = 1{,}000$. Because f_{abs} and N_{surf} are comparable to the values for athermal phonons (Section 5.2), the resulting requirement is similar, $f_{surf} \approx 0.01$. The energy resolution calculation is also analogous, with τ_{ph} replaced by the substrate quasiparticle lifetime τ_{qp}^{subs}.

There was significant work on superconducting substrates in the 1980s and 1990s using SIS tunnel junction sensors, but it was abandoned in favor of techniques capable of discriminating nuclear from electron recoils. The recent renewal of interest has not yet yielded results.

5.6. Superfluid Helium: Phonons, Rotons, and Quantum Evaporation

Superfluid ^{4}He was proposed for solar neutrino detection (109) and has had a resurgence as a DM detector (110–112). Energy deposition in superfluid ^{4}He produces a rich set of excitations, which can be exploited for DM searches. These include singlet diatomic molecules (excimers), triplet excimers, rotons, and phonons. The singlet and triplet scintillation channels are available only for energy depositions above the 19.77-eV band gap. Rotons and phonons are the only remaining excitations below the band gap. For DM searches below 100 MeV/c^2, the nuclear recoil signal spectrum lies entirely below the 19.77-eV band gap. In addition, for a ^{4}He detector with a liquid–vacuum interface, there is a quantum evaporation threshold of 0.62 meV, meaning that atoms from the superfluid can be ejected into the vacuum if phonons or rotons with energy above this threshold impinge on the surface. The probability of quantum evaporation for each surface interaction depends on the angle and momentum of the incident phonon or roton.

The above-cited authors provide several methods to read out excitations, including TES devices immersed in the ^{4}He that would be sensitive to all excitations, a TES wafer located above the liquid surface that would detect the atoms from quantum evaporation events, and the use of a field ionization technique that would first ionize the ejected atoms and then accelerate them into a calorimeter. With projected sensor thresholds down to 1 meV and/or the ability to sense individual ^{4}He evaporated atoms, these detectors would be sensitive to DM with a mass of $\mathcal{O}(\text{keV}/c^2)$ and above (**Figure 2**).

For energy depositions below the gap, no scintillation is possible, but the phonon and roton channels are still available. One notable background below 1-eV recoils is coherent photon–nucleus scattering, which can be controlled by effective shielding. A large ^{4}He detector would also be sensitive to solar neutrinos through the CEνNS process (the neutrino floor; see **Figure 2**).

[16]The barrier must be thick enough ($\gtrsim$ tens of nanometers) to prevent quasiparticle tunneling. To mitigate the additional acoustic mismatch, it could be tuned for constructive interference near 2Δ. For an Al substrate and amorphous alumina barrier, $2\,\Delta_{Al} \approx (100\text{ GHz})\,h \sim hc_{AlOx}/(100\text{ nm})$.

[17]$v_F \approx 2{,}000\text{ km s}^{-1}$ in Al, but the group velocity decreases near Δ in superconductors (107, 108).

5.7. Cutting-Edge Approaches

Condensed matter systems, and especially novel materials developed recently, are replete with meV-scale excitations. We review two such excitations that have been studied for particle detection.

5.7.1. Dirac materials. Dirac materials are semiconductors in which the electron band structure yields a linear dispersion relation in specific regions of momentum space, like a relativistic Dirac fermion. Their potential as quantum sensors arises from the fact that a small gap can open at the point where the electron and hole bands would nominally meet, yielding a much lower electron–hole pair excitation energy (e.g., 30 meV in $ZrTe_5$) than in conventional semiconductors. They are therefore an excellent candidate for electron–hole pair architectures (Section 5.4) with much lower thresholds for electron scattering and bosonic absorption than those of conventional semiconductors and insulators like Si, Ge, and diamond (113).

Dirac materials have an additional feature relevant for DM detection: The linear dispersion relation combines with the quadratic DM dispersion relation to yield strong directional dependence, which we argue would be very useful for signal–background discrimination (see Section 5.1.3) (84, 114). (As far as we know, the implications of this feature for neutrino scattering have not been explored.) These materials are quite novel, and work is ongoing to measure their properties (in particular, their dielectric loss function) and to fabricate sensors on them.

5.7.2. Magnons. Magnons are the electron-spin equivalent of phonons: They are a wave in the spin ordering of magnetically ordered materials, corresponding to precession of the electron magnetic moment about the nominal magnetic moment axis. They have dispersion relations and energies similar to those of phonons. Their main utility would be for the detection of DM or neutrinos interacting via a spin-dependent coupling (the nonrelativistic limit of magnetic dipole, anapole, and pseudomediated couplings), which may not couple well to other excitations (115). While there have been calculations, there has not yet been any experimental exploration of such materials. They must have magnetic order, which generally requires incorporation of heavy elements, and so radiopurity would be a significant concern. It is also not yet clear what sensor would be compatible with them.

6. QUANTUM SENSING IN SENSOR READOUT

KID sensitivity can be limited by amplifier noise, especially as single-quasiparticle sensitivity is sought. QIS techniques may provide solutions.

6.1. The Haus–Caves Theorem and Quantum Limits on Amplifier Noise

The Haus–Caves theorem (116) states that a phase-insensitive amplifier—one that amplifies its input electromagnetic (EM) signal independently of the phase of the input—always adds noise in both quadratures,[18] with equivalent amplifier noise temperature

$$k_B T_N^{amp} = \frac{1}{2}\left|1 - \frac{1}{G}\right| h f_0 \xrightarrow{G \gg 1} \frac{1}{2} h f_0, \qquad 11.$$

[18] "Quadratures" refers to the two complementary observables of the EM field relative to a phase reference: One quadrature is the component having the same phase as the reference [in-phase (I) component], and the other quadrature is the component 90° out of phase with the reference [quadrature (Q) component]. These quadratures are a (perhaps trivial) linear combination of the complementary, noncommuting amplitude and phase observables typically associated with the EM field. The phase reference is arbitrary and is set by the system of interest.

where G is the square of the magnitude of the voltage gain, which is obviously always much larger than unity. Fundamentally, the theorem is due to the Heisenberg uncertainty relation, which applies to the two quadratures of any EM mode (amplitude and phase or real and imaginary) as it does to the momentum and position of a particle. If we designate the input EM mode quadratures as X_1 and X_2 and the output quadratures as Y_1 and Y_2, the Haus–Caves theorem arises from the fact that (Y_1, Y_2) are obtained from (X_1, X_2) by the addition of internal modes (F_1, F_2) of the amplifier (the gain mechanism). The uncertainties on (F_1, F_2) thus add to the uncertainties on (X_1, X_2) to yield uncertainties on (Y_1, Y_2) larger than those on (X_1, X_2) (all quantities referred to the amplifier input). Since the amplifier is phase insensitive, the uncertainties must increase by the same amount for both quadratures. The minimum variance result is that each quadrature's variance increases additively by exactly the Haus–Caves theorem amount.

In addition to the amplifier-added noise, the vacuum transmitted to the amplifier from the matched load it views—usually, the last cryogenic[19] attenuator before the nondissipative device being monitored—has "vacuum noise," $k_B T_N^{vac} = hf_0/2$, in each quadrature due to the EM field's zero-point energy. Thus, the minimum noise temperature achievable with a phase-insensitive amplifier is the SQL:[20]

$$k_B T_N = k_B T_N^{vac} + k_B T_N^{amp} = hf_0. \qquad 12.$$

We are aware of four amplifier configurations that have approached or reached the SQL: the microstrip SQUID amplifier (MSA; 117), the Josephson parametric amplifier (JPA; e.g., 118, 119), the traveling-wave JPA (TWJPA; e.g., 120), and the traveling-wave kinetic inductance parametric amplifier (TWKPA) (121–123). Any of these options could read out a single KID, while both the TWJPA and TWKPA are compatible with readout of an array of KIDs; a TWKPA demonstration (albeit not reaching the SQL) is provided in Reference 124.

6.2. Gymnastics with the Haus–Caves Theorem: Vacuum Squeezing and Squeezed Amplification

It is possible to circumvent, in a sense, the SQL via use of a phase-sensitive amplifier, which is an amplifier that treats its two input quadratures differently, with gains G_1 and G_2. If one requires $G_1 G_2 = 1$, so that one quadrature is amplified and the other attenuated, then one can show that (X_1, X_2) and (Y_1, Y_2) satisfy the same uncertainty relation (referred to input)—no added uncertainty—implying noiseless gain in one quadrature ($G_1 > 1$ for specificity) and noiseless attenuation ($G_2 = 1/G_1 < 1$) in the other. Nevertheless, vacuum noise persists, and the improvement over the SQL in each quadrature would be only a factor of 2.[21] Vacuum noise can be reduced, however, by using another phase-sensitive amplifier, applied to the vacuum incident on the nondissipative device and the amplifier, to now noiselessly attenuate the quadrature of interest and thus its vacuum noise. With the two phase-sensitive amplifiers, one squeezing the vacuum incident on the

[19] $T_{atten} \ll hf_0/k_B$, so its thermal emission is negligible.

[20] The SQL is colloquially termed "one photon of noise," coming from "half a photon of vacuum noise" and "half a photon of added amplifier noise." This terminology arises because an amplifier noise temperature T_N implies a noise power $k_B T_N$ J s^{-1} Hz^{-1} $= k_B T_N$ W Hz^{-1}, where Hz^{-1} refers to input spectral bandwidth. When $k_B T_N$ is written in terms of multiples of hf_0, the interpretation becomes photons per second per hertz, which one abbreviates as a "number of photons" because the per-second and per-hertz units cancel one another.

[21] There would, in fact, be no improvement if the signal appears equally in the two quadratures since one is now lost.

device and the other amplifying the squeezed quadrature only, both vacuum and amplifier-added noise can in principle be reduced.

This concept is motivated by the success in implementing the corresponding architecture in the HAYSTAC axion-search experiment, in which a physical RF cavity is the nondissipative device and JPAs (125) are used. A total noise temperature improvement of 2.8 beyond the SQL has been demonstrated (126). The concept should be applicable with traveling-wave amplifiers, and Reference 127 has worked out how to do phase-sensitive amplification with a TWKPA. We note that this general technique has also been applied on a wide range of QIS and precision measurement platforms, including LIGO (128).

There are two potential challenges to this implementation with KIDs. First, loss in the connections between the elements inevitably degrades both types of squeezing, making it difficult to exceed the SQL by more than ∼10 dB. Second, loss in the resonator ($Q_i \ll \infty$) may degrade the squeezed vacuum as it is transmitted to the squeezed amplifier, although, in Reference 126, 0.5 dB of loss attributed to the cavity was additive.

6.3. Qubit-Based Readout and Radio Frequency Photon Counting

Photon counting is the logical limit of the above: It eliminates vacuum noise because no real photons are emitted by vacuum noise (infinite vacuum squeezing), and there is no added amplifier noise in the limit such that the photon detection threshold is well below a single photon (noiseless amplification). Photon counting is much more robust against loss in the transmission network than vacuum squeezing because zero-point fluctuations of lossy components add noise but do not yield real photons.

Various qubit-based RF-photon-counting techniques have been demonstrated in the literature. We describe one example that may be applicable for KID readout (129). The authors demonstrated a technique using CPB qubits for photon counting applicable to RF-cavity axion searches, in which an axion DM particle combines with a virtual photon from a magnetic field to create an RF photon in a cavity resonant with the axion mass. This approach relies on the CPB charge state's dependence on resonator photon number in the Jaynes–Cummings Hamiltonian (as opposed to the resonator's f_r dependence on CPB charge state; see Section 4.4.1). The CPB is now coupled to two 3-dimensional RF cavities: an axion-detection cavity and a readout cavity (the latter replacing the superconducting resonator). Creation of an axion in the first cavity modifies the charge state of the CPB, which is then observed via the shift in *readout cavity* resonant frequency f_r^r. The cooled axion cavity (f_r^c with $T \ll h f_r^c / k_B$) has exponentially suppressed thermal emission of real photons, and the cavity's vacuum noise does not yield real photons, so the appearance of a shift in f_r^r corresponds to unambiguous detection of a photon at f_r^c in the axion cavity. For KIDs, the operating mode would be to replace the cavities with superconducting resonators, apply a nulling tone after the KID to zero the quiescent photon number on the transmission line, and feed that nulled signal to the axion-cavity equivalent. A quasiparticle density change in the KID would modify its transmission so that the nulling would become imperfect and a photon or photons would reach the axion-cavity equivalent.

SUMMARY POINTS

1. Dark matter (DM) direct detection and many topics in neutrino physics can benefit from the ability to sense depositions down to meV energies.

2. Both techniques drawn from quantum information science (QIS) and from historical efforts in DM and neutrino detection have the potential to yield quantum sensors capable of sensing these small energy depositions, down to the level of single condensed matter quanta like phonons, rotons, magnons, and electron–hole pairs.
3. Application of quantum sensors requires an understanding of the quantum sensing component, of how excitations are produced by DM or neutrinos, and of how the two can be coupled.
4. QIS techniques may also be applicable for readout to enable quantum sensors to detect single quanta.

FUTURE ISSUES

1. Numerous challenges are already visible in the effort to reach detection of meV quanta: residual gapped excitations, decoupled or parasitic heat capacities, nonideal loss mechanisms, and others.
2. The backgrounds at meV–eV energies are poorly understood, requiring more theoretical and experimental investigation.
3. Gram-scale detectors based on quantum sensors will require extensive multiplexing to reach kilogram-year exposures, a challenge that has not been fully addressed yet.

DISCLOSURE STATEMENT

E.F.-F. and S.R.G. receive funding from the US Department of Energy (DOE) and the National Science Foundation to undertake work discussed in this review. E.F.-F. and S.R.G. are members of the SuperCDMS SNOLAB Collaboration and participate in the SuperCDMS SNOLAB experiment, which benefits from techniques described in this review. S.R.G. participated in the DOE Basic Research Needs study (1) cited in this review.

ACKNOWLEDGMENTS

The authors acknowledge an uncountable number of conversations with experts in the topics covered in this review over the years, with special thanks to (in alphabetical order) Rana Adhikari, Blas Cabrera, Aaron Chou, Peter Day, Jiansong Gao, Kent Irwin, Nikita Klimovich, Noah Kurinsky, Konrad Lehnert, Omid Noroozian, Matt Pyle, Karthik Ramanathan, Bernard Sadoulet, Tanner Trickle, Kevin (Zhengkang) Zhang, Jonas Zmuidzinas, and Kathryn Zurek. They acknowledge support from the US Department of Energy, NASA, the National Science Foundation, and their home institutions.

LITERATURE CITED

1. Fleming B, Shipsey I, co-chairs. *Basic research needs for high energy physics detector research & development*. Rep., US Dep. Energy, Washington, DC. **https://science.osti.gov/-/media/hep/pdf/Reports/2020/DOE_Basic_Research_Needs_Study_on_High_Energy_Physics.pdf?la=en&hash=A5C00A96314706A0379368466710593A1A5C4482** (2019)

2. Strigari LE. *Phys. Rep.* 531(1):1 (2013)
3. Bertone G, Hooper D. *Rev. Mod. Phys.* 90(4):045002 (2018)
4. Battaglieri M, et al. arXiv:1707.04591 [hep-ph] (2017)
5. Lee BW, Weinberg SW. *Phys. Rev. Lett.* 39:165 (1977)
6. Peccei RD, Quinn HR. *Phys. Rev. Lett.* 38(25):1440 (1977)
7. Peccei RD, Quinn HR. *Phys. Rev. D* 16(6):1791 (1977)
8. Weinberg S. *Phys. Rev. Lett.* 40(4):223 (1978)
9. Wilczek F. *Phys. Rev. Lett.* 40(5):279 (1978)
10. Preskill J, Wise MB, Wilczek F. *Phys. Lett. B* 120(1–3):127 (1983)
11. Dine M, Fischler W. *Phys. Lett. B* 120(1–3):137 (1983)
12. Abbott LF, Sikivie P. *Phys. Lett. B* 120(1–3):133 (1983)
13. Lewin JD, Smith PF. *Astropart. Phys.* 6:87 (1996)
14. Griffin SM, et al. *Phys. Rev. D* 101(5):055004 (2020)
15. Fukuda S, et al. *Phys. Rev. Lett.* 86(25):5656 (2001)
16. Ahmad QR, et al. *Phys. Rev. Lett.* 89(1):011301 (2002)
17. Fukuda Y, et al. *Phys. Rev. Lett.* 81(8):1562 (1998)
18. Eguchi K, et al. *Phys. Rev. Lett.* 90(2):021802 (2003)
19. Araki T, et al. *Phys. Rev. Lett.* 94(8):081801 (2005)
20. Ahn MH, et al. *Phys. Rev. Lett.* 90(4):041801 (2003)
21. Michael DG, et al. *Phys. Rev. Lett.* 97(19):191801 (2006)
22. Group PD, et al. *Prog. Theor. Exp. Phys.* 2020(8):083C01 (2020)
23. Formaggio JA, de Gouvêa ALC, Robertson RGH. *Phys. Rep.* 914:1 (2021)
24. Aker M, et al. *Phys. Rev. Lett.* 123(22):221802 (2019)
25. Freedman DZ. *Phys. Rev. D* 9(5):1389 (1974)
26. Cowan CL Jr., et al. *Science* 124(3212):103 (1956)
27. Akimov D, et al. (COHERENT Collab.) *Science* 357(6356):1123 (2017)
28. Akimov D, et al. (COHERENT Collab.) arXiv:2110.07730 [hep-ex] (2021)
29. Akimov D, et al. (COHERENT Collab.) *Phys. Rev. Lett.* 126(1):012002 (2021)
30. Bhupal Dev PS, et al. *SciPost Phys. Proc.* 2:001 (2019)
31. Coloma P, et al. *J. High Energy Phys.* 2002:23 (2020)
32. Orebi Gann GD, Zuber K, Bemmerer D, Serenelli A. *Annu. Rev. Nucl. Part. Sci.* 71:491 (2021)
33. Billard J, Strigari LE, Figueroa-Feliciano E. *Phys. Rev. D* 91(9):095023 (2015)
34. Cerdeño DG, et al. *J. High Energy Phys.* 1605:118 (2016)
35. Essig R, Sholapurkar M, Yu TT. *Phys. Rev. D* 97(9):095029 (2018)
36. Bœhm C, et al. *J. Cosmol. Astropart. Phys.* 1901:043 (2019)
37. Sierra DA, Dutta B, Liao S, Strigari LE. *J. High Energy Phys.* 1912:124 (2019)
38. Strigari LE. *Phys. Rev. D* 93(10):103534 (2016)
39. Yanagisawa C. *Front. Phys.* 2:30 (2014)
40. Baracchini E, et al. arXiv:1808.01892 [physics.ins-det] (2018)
41. Betti MG, et al. *J. Cosmol. Astropart. Phys.* 1907:047 (2019)
42. Van Duzer T, Turner CW. *Principles of Superconductive Devices and Circuits*. Upper Saddle River, NJ: Prentice Hall. 2nd ed. (1998)
43. Sakai K, et al. *J. Low Temp. Phys.* 199(3–4):949 (2020)
44. Ren R, et al. *Phys. Rev. D* 104(3):032010 (2021)
45. Battistelli ES, et al. *Eur. Phys. J. C* 75:353 (2015)
46. Doriese WB, et al. *J. Low Temp. Phys.* 184(1–2):389 (2016)
47. Morgan KM, et al. *Appl. Phys. Lett.* 109(11):112604 (2016)
48. Mates JAB, et al. *Appl. Phys. Lett.* 111(6):062601 (2017)
49. Irwin KD, et al. *J. Low Temp. Phys.* 193(3–4):476 (2018)
50. Irwin KD, Lehnert KW. *Appl. Phys. Lett.* 85(11):2107 (2004)
51. Henderson SW, et al. In *Proceedings of SPIE*, Vol. 10708: *Millimeter, Submillimeter, and Far-Infrared Detectors and Instrumentation for Astronomy IX*, ed. J Zmuidzinas, JR Gao, Paper 1070819. Bellingham, WA: SPIE (2018)

52. Zmuidzinas J. *Annu. Rev. Condens. Matter Phys.* 3:169 (2012)
53. Mazin BA, et al. In *Proceedings of SPIE*, Vol. 4849: *Highly Innovative Space Telescope Concepts*, ed. HA MacEwen, pp. 283–93. Bellingham, WA: SPIE (2002)
54. Day PK, et al. *Nature* 425:817 (2003)
55. Doyle S, et al. *J. Low Temp. Phys.* 151(1–2):530 (2008)
56. Duan R, et al. 2010. In *Proceedings of SPIE*, Vol. 7741: *Millimeter, Submillimeter, and Far-Infrared Detectors and Instrumentation for Astronomy V*, ed. WS Holland, J Zmuidzinas, Paper 77411V. Bellingham, WA: SPIE
57. Duan R, Golwala S. 2020. In *Proceedings of SPIE*, Vol. 11453: *Millimeter, Submillimeter, and Far-Infrared Detectors and Instrumentation for Astronomy X*, ed. J Zmuidzinas, J-R Gao, Paper 114531Z. Bellingham, WA: SPIE
58. Gordon S, et al. *J. Astron. Instrum.* 5(4):1641003 (2016)
59. Bourrion O, et al. *J. Instrum.* 11(11):P11001 (2016)
60. van Rantwijk J, et al. *IEEE Trans. Microw. Theory Tech.* 64(6):1876 (2016)
61. de Visser PJ, Withington S, Goldie DJ. *J. Appl. Phys.* 108:114504 (2010)
62. de Visser PJ, et al. *Appl. Phys. Lett.* 100(16):162601 (2012)
63. de Visser PJ, et al. *Phys. Rev. Lett.* 112:047004 (2014)
64. Bueno J, et al. *Appl. Phys. Lett.* 105:192601 (2014)
65. de Rooij SAH, et al. *Phys. Rev. B* 104(18):L180506 (2021)
66. Baselmans J, Yates S, Diener P, Visser P. *J. Low Temp. Phys.* 167(3–4):360 (2012)
67. Gao J, et al. *Appl. Phys. Lett.* 90:2507 (2007)
68. Gao J, et al. *Appl. Phys. Lett.* 92:2505 (2008)
69. Gao J, et al. *Appl. Phys. Lett.* 92:212504 (2008)
70. Gao J. *The physics of superconducting microwave resonators*. PhD Thesis, Calif. Inst. Technol., Pasadena (2008)
71. Esmaeil Zadeh I, et al. *Appl. Phys. Lett.* 118(19):190502 (2021)
72. You L. *Nanophotonics* 9(9):2673 (2020)
73. Hochberg Y, et al. *Phys. Rev. Lett.* 123(15):151802 (2019)
74. Bouchiat V, et al. *Phys. Scr.* T76(1):165 (1998)
75. Blais A, et al. *Phys. Rev. A* 69(6):062320 (2004)
76. Wallraff A, et al. *Nature* 431(7005):162 (2004)
77. Shaw MD, et al. *Phys. Rev. B* 79(14):144511 (2009)
78. Echternach PM, Pepper BJ, Reck T, Bradford CM. *Nat. Astron.* 2:90 (2018)
79. Holmström E, Kuronen A, Nordlund K. *Phys. Rev. B* 78(4):045202 (2008)
80. Trickle T, et al. *J. High Energy Phys.* 2003:36 (2020)
81. Hochberg Y, et al. *Phys. Rev. Lett.* 127(15):151802 (2021)
82. Kadribasic F, et al. *Phys. Rev. Lett.* 120(11):111301 (2018)
83. Griffin S, Knapen S, Lin T, Zurek KM. *Phys. Rev. D* 98(11):115034 (2018)
84. Coskuner A, Mitridate A, Olivares A, Zurek KM. *Phys. Rev. D* 103(1):016006 (2021)
85. Hochberg Y, Pyle M, Zhao Y, Zurek KM. *J. High Energy Phys.* 1608:57 (2016)
86. Mitridate A, Trickle T, Zhang Z, Zurek KM. *J. High Energy Phys.* 2109:123 (2021)
87. Hochberg Y, Lin T, Zurek KM. *Phys. Rev. D* 94(1):015019 (2016)
88. Gelmini GB, Takhistov V, Vitagliano E. *Phys. Lett. B* 809:135779 (2020)
89. Robinson AE. *Phys. Rev. D* 95(2):021301 (2017)
90. Amaral DW, et al. *Phys. Rev. D* 102(9):091101 (2020)
91. Du P, Egana-Ugrinovic D, Essig R, Sholapurkar M. *Phys. Rev. X* 12(1):011009 (2022)
92. Leman SW. *Rev. Sci. Instrum.* 83(9):091101 (2012)
93. Zadeh LA, Ragazzini JR. *Proc. IRE* 40(10):1223 (1952)
94. Pyle M. *Optimizing the design and analysis of cryogenic semiconductor dark matter detectors for maximum sensitivity*. PhD Thesis, Stanford Univ., Stanford, CA (2012)
95. Kurakado M. *Nucl. Instrum. Methods A* 196:275 (1982)
96. Kozorezov AG, et al. *Phys. Rev. B* 611:11807 (2000)

97. Fink CW, et al. *Appl. Phys. Lett.* 118(2):022601 (2021)
98. Rothe J, et al. *J. Low Temp. Phys.* 199(1–2):433 (2020)
99. Chen R, Figueroa-Feliciano E, Schmidt B. arXiv:2111.05757 [physics.ins-det] (2021)
100. Baulieu G, et al. arXiv:2111.10308 [physics.ins-det] (2021)
101. Tiffenberg J, et al. *Phys. Rev. Lett.* 119(13):131802 (2017)
102. Barak L, et al. *Phys. Rev. Lett.* 125(17):171802 (2020)
103. Barak L, et al. *Phys. Rev. Appl.* 17(1):014022 (2022)
104. Neganov BS, Trofimov VN. *JETP Lett.* 28:328 (1978)
105. Luke PN. *J. Appl. Phys.* 64:6858 (1988)
106. Agnese R, et al. *Phys. Rev. Lett.* 121(5):051301 (2018)
107. Bardeen J, Cooper LN, Schrieffer JR. *Phys. Rev.* 108(5):1175 (1957)
108. Ullom JN, Fisher PA, Nahum M. *Phys. Rev. B* 58(13):8225 (1998)
109. Lanou RE, Maris HJ, Seidel GM. *Phys. Rev. Lett.* 58(23):2498 (1987)
110. Maris HJ, Seidel GM, Stein D. *Phys. Rev. Lett.* 119(18):181303 (2017)
111. Hertel SA, et al. *Phys. Rev. D* 100(9):092007 (2019)
112. Liao J, et al. arXiv:2103.02161 [astro-ph.IM] (2021)
113. Hochberg Y, et al. *Phys. Rev. D* 97(1):015004 (2018)
114. Geilhufe RM, Kahlhoefer F, Winkler MW. *Phys. Rev. D* 101(5):055005 (2020)
115. Trickle T, Zhang Z, Zurek KM. *Phys. Rev. Lett.* 124(20):201801 (2020)
116. Caves CM. *Phys. Rev. D* 26:1817 (1982)
117. Mück M, et al. *Appl. Phys. Lett.* 72(22):2885 (1998)
118. Siddiqi I, et al. *Phys. Rev. Lett.* 93(20):207002 (2004)
119. Castellanos-Beltran MA, Lehnert KW. *Appl. Phys. Lett.* 91(8):083509 (2007)
120. Macklin C, et al. *Science* 350(6258):307 (2015)
121. Eom BH, Day PK, Leduc HG, Zmuidzinas J. *Nat. Phys.* 8:623 (2012)
122. Chaudhuri S, et al. *Appl. Phys. Lett.* 110:152601 (2017)
123. Vissers MR, et al. *Appl. Phys. Lett.* 108(1):012601 (2016)
124. Zobrist N, et al. *Appl. Phys. Lett.* 115(4):042601 (2019)
125. Castellanos-Beltran MA, Irwin KD, Hilton GC, Vale LR, Lehnert KW. *Nat. Phys.* 4:929 (2008)
126. Malnou M, et al. *Phys. Rev. X* 9(2):021023 (2019)
127. Shu S, et al. *Phys. Rev. Res.* 3(2):023184 (2021)
128. Aasi J, et al. *Nat. Photonics* 7(8):613 (2013)
129. Dixit AV, et al. *Phys. Rev. Lett.* 126(14):141302 (2021)
130. Chang Y-Y, et al. *J. Low Temp. Phys.* 193(5–6):1199 (2018)

Annual Review of Nuclear and Particle Science

Volume 72, 2022

Contents

Errata

An online log of corrections to *Annual Review of Nuclear and Particle Science* articles may be found at http://www.annualreviews.org/errata/nucl